Sandwich-Structured Ordered Mesoporous Polydopamine/MXene Hybrids as High-Performance Anodes for Lithium-Ion Batteries

Tao Li,[a,b+] Bing Ding,[a,c+] Jie Wang,[a*] Zongyi Qin,[b] Joseph F. S. Fernando,[d] Yoshio Bando,[a] Ashok Kumar Nanjundan,[e] Yusuf Valentino Kaneti,[a,e] Dmitri Golberg,[a,d*] and Yusuke Yamauchi[e,f*]

[a] International Research Center for Materials Nanoarchitechtonics (WPI-MANA), National Institute for Materials Science (NIMS), 1-1 Namiki, Tsukuba, Ibaraki 305-0044, Japan

[b] State Key Laboratory for Modification of Chemical Fibers and Polymer Materials, and College of Material Science and Engineering, Donghua University, Shanghai 201620, China

[c] Jiangsu Key Laboratory of Electrochemical Energy-Storage Technologies, College of Materials Science and Technology, Nanjing University of Aeronautics and Astronautics, Nanjing 210016, China

[d] School of Chemistry, Physics and Mechanical Engineering, Science and Engineering Faculty, Queensland University of Technology (QUT), Brisbane, Queensland, 4000, Australia

[e] School of Chemical Engineering and Australian Institute for Bioengineering and Nanotechnology (AIBN), The University of Queensland, Brisbane, QLD 4072, Australia

[f] Department of Plant & Environmental New Resources, Kyung Hee University, 1732 Deogyeong-daero, Giheung-gu, Yongin-si, Gyeonggi-do 446-701, South Korea

+ These authors equally contributed to this work.

E-mails: WANG.Jie@nims.go.jp; dmitry.golberg@qut.edu.au; y.yamauchi@uq.edu.au

Abstract

Organic polymers have attracted significant interest as electrodes for energy storage devices due to their advantages, including molecular flexibility, cost-effectiveness, and environmentally-friendly nature. Nevertheless, the real implementation of polymer-based electrodes is restricted by their poor stability, low capacity, and slow electron transfer/ion diffusion kinetics. In this work, a sandwich-structured composite of ordered mesoporous polydopamine (OMPDA)/$Ti_3C_2T_x$ has been fabricated by *in situ* polymerization of dopamine on the surface of $Ti_3C_2T_x$ by employing PS-*b*-PEO block polymer as a soft template. The OMPDA layers with vertically oriented, accessible nanopores (~20 nm) provide a continuous pore channel for ion diffusion, while the $Ti_3C_2T_x$ layers guarantee a fast electron transfer path. The OMPDA/$Ti_3C_2T_x$ composite anode exhibits high reversible capacity, good rate performance, and excellent cyclability for lithium-ion batteries. The *in situ* transmission electron microscopy analysis reveals that the OMPDA in the composite only shows a small volume expansion and almost preserves the initial morphology during lithiation. Moreover, these *in situ* experiments also demonstrate the generation of a stable and ultrathin solid electrolyte interphase (SEI) layer surrounding the active material, which acts as an electrode protective film during cycling. This study demonstrates the method to develop polymer-based electrodes for high-performance rechargeable batteries.

Keywords: Ordered mesoporous polydopamine; MXene; Sandwich structure; Lithium-ion batteries; In situ transmission electron microscopy

Introduction

As the most popular energy storage device on the market, lithium-ion batteries (LIBs) are widely used in portable electronics, electric vehicles, and stationary electricity storage applications.[1-7] Although many pieces of researches have been performed to optimize the electrode design, the fabrication of LIB electrodes with high energy density, high power density, and good cyclability remains a challenge.[8-11] Organic electrode materials are heralded as alternative electrodes for LIBs because of their advantages, including molecular flexibility, cost-effectiveness, and environmental friendliness.[12-15] During the redox reactions of organic electrodes, functional groups, such as carboxylate and thioether, usually act as redox centers for alkali-metal ions, while the aromatic cores are responsible for electron donation and acceptance.[16-18] Carbonyl compounds, with quinone or derivatives of aromatic carboxylic acid as active centers, have received substantial research attention as high-performance polymer-based electrodes.[19-23] However, their practical implementation is restricted by their small reversible capacity, limited rate performance, and poor cyclability.

Polydopamine (PDA), which is prepared by the polymerization of dopamine (DA), is an ideal polymer with redox-active properties. Theoretically, during the discharge process, PDA can accommodate eleven Li^+ ions in one active unit through quinone groups and this gives rise to a high theoretical capacity up to 2006 mAh g^{-1}.[24,25] However, a limited amount of quinone is typically formed during the self-polymerization reaction of DA, therefore greatly restricting the capacity of PDA electrode. Zhang *et al.* found that the content of quinone could be increased by enhancing the oxidation degree of PDA.[24] However, the oxidation reaction will certainly reduce the electronic conductivity of PDA, leading to a reduction in electrochemical performance.[17,26] In general, the electronic conductivity of polymers can be improved by polymerizing redox-active molecules on conductive substrates and forming core-shell heterostructures.[27-29] In such hybrid architectures, the conductive substrates can provide a higher electronic conductivity, while the bonding of molecules *via* covalent bonds can prevent the fragmenting of molecules. Carbon materials (*e.g.*, graphene and carbon nanotubes (CNT)) are the most frequently used substrates for polymers due to their high conductivity, low cost, and morphological variety.[30-32] Utilizing this strategy, Jang and Lee successfully coated PDA on the surface of CNT.[29] When applied in LIBs, the hybrid PDA-CNT electrode exhibited greatly improved performance compared to pure PDA material. However, most carbon materials are not suitable electrodes for LIBs due to their limited lithium-ion storage performance. The combination of polymer with carbon will sacrifice the overall gravimetric capacity of the whole composite. It is expected that another highly conductive material with superior Li-

storage performance will be a better candidate for hybridization with PDA to achieve better overall performance.

The ordered mesoporous structure has been proven to be effective in providing ion transfer paths and facilitating the ion-diffusion kinetics within an electrode. Furthermore, the mesoporous structure can promote better penetration of electrolyte ions and guarantee efficient ion transfer within the electrode, leading to high electrochemical performance even at high rates.[33,34] Especially, the combination of mesopores with a two-dimensional (2D) morphology can further shorten the diffusion pathways and increase the accessible surface area for lithium ions in the active material. 2D ordered mesoporous carbon and TiO_2 prepared by using block copolymers as templates, have been demonstrated to be superior over their bulk counterparts for LIB applications.[35-37] Nevertheless, 2D ordered mesoporous polymers prepared by using block copolymers as templates have been rarely reported. It is expected that, by combining the advantages of each component, a hybrid composite of mesoporous polymer and 2D conductive material with large reversible capacity, good rate performance, and satisfactory cycling life can be achieved.

In this report, we prepare a novel sandwich-structured ordered mesoporous polydopamine (OMPDA)/MXene ($Ti_3C_2T_x$) composite by direct polymerization of DA on the outer surface of $Ti_3C_2T_x$ nanosheets, which forms a new kind of LIB anode with high electrochemical performance.[38,39] By employing PS-*b*-PEO block copolymer as a soft template, vertically-oriented (~20 nm in diameter) nanopores are created to obtain mechanically stable OMPDA thin films. The OMPDA layers with accessible nanopores (~20 nm) provide continuous pore channels for ion diffusion, while the $Ti_3C_2T_x$ layers guarantee fast electron transfer, leading to the greatly enhanced lithium storage performance of OMPDA/$Ti_3C_2T_x$ relative to pristine OMPDA and smooth PDA (SPDA)/$Ti_3C_2T_x$ complex without pores when applied in LIBs. At 50 mA g^{-1}, the OMPDA/$Ti_3C_2T_x$ electrode can achieve a specific capacity up to ~1000 mAh g^{-1}. Even at 1 A g^{-1}, a relatively large capacity of ~430 mAh g^{-1} is still maintained after 600 cycles. Moreover, *in situ* analysis by transmission electron microscope has been conducted to observe the changes in the electrode structure upon the charge/discharge process.

Results and discussion

Structural characterizations

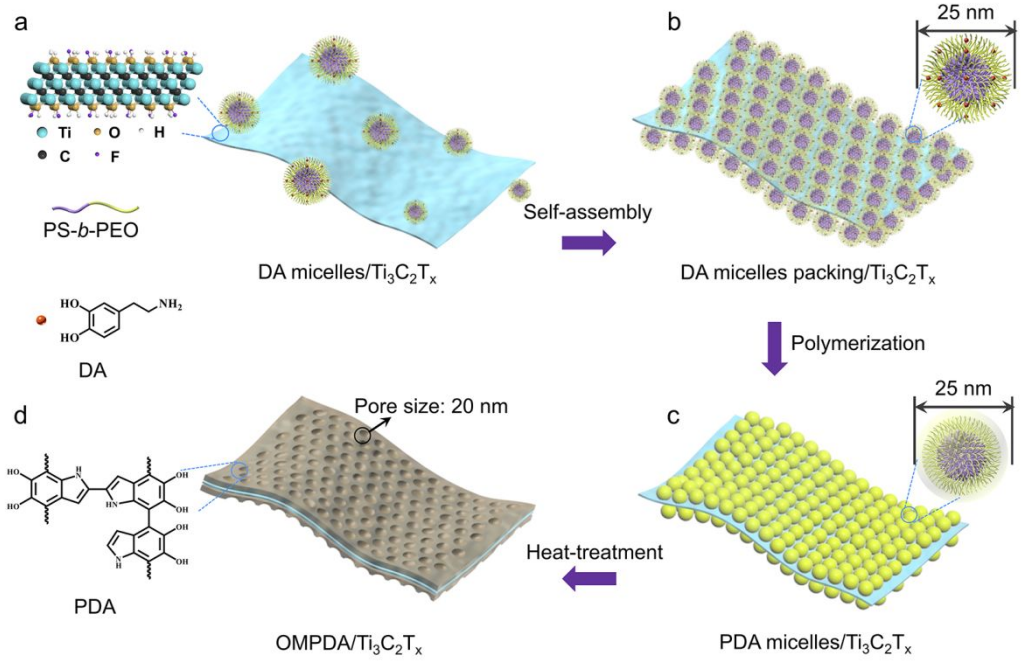

Figure 1. Schematic drawing depicting the preparation steps of OMPDA/$Ti_3C_2T_x$ composite: (a) Mixing the DA micelles with $Ti_3C_2T_x$ nanosheets, (b) packing of DA micelles and subsequent (c) direct polymerization of PDA micelles on the surface of $Ti_3C_2T_x$ nanosheets, and (d) obtaining the OMPDA/$Ti_3C_2T_x$ after heat-treatment.

The preparation process of OMPDA/$Ti_3C_2T_x$ is provided in **Figure 1**. $Ti_3C_2T_x$ nanosheets prepared by etching Ti_3AlC_2 followed by exfoliation are used as a substrate for the growth of DA. First, the solution of PS-*b*-PEO in tetrahydrofuran and the solution of dopamine in ethanol/water (volume ratio of ethanol and water is 1:1) mixture are mixed under mild stirring. Following the micellization of PS-*b*-PEO in the mixed solvent,[40-41] DA micelles (DAmi) composed of dopamine molecules and PS-*b*-PEO are initially formed by self-assembly process (**Figure 1a**). After the addition of the solution containing $Ti_3C_2T_x$ nanosheets, DAmi can interact with $Ti_3C_2T_x$ through a hydrogen bond formed between the catechol/quinone groups of DA and $^-$OH and $^-$F terminal groups of $Ti_3C_2T_x$ (**Figure 1b**). As shown in **Figure S1a**, the DAmi are uniformly assembled on the surface of the $Ti_3C_2T_x$ nanosheets. After stirring for 2 h, an ammonia solution was added to initiate the polymerization of DAmi (**Figure 1c**). The average size of PDA/PS-*b*-PEO micelles (PDAmi) on the surface of $Ti_3C_2T_x$ nanosheets remains around 25 nm even after completion of the polymerization process (**Figure 2a-b** and **Figure S1b-f**). The cross-sectional TEM images (**Figure 2c** and **Figure S2**) show that a layer of

PDAmi is formed onto both sides of the substrate with the thickness being around 15 nm, thereby creating a sandwich-like structure. The elemental mapping results demonstrate that the elements N, C, O, F, and Ti are homogeneously distributed throughout the sandwich structure (**Figure S3**), indicating the uniform coating of the surface of $Ti_3C_2T_x$ nanosheets by PDAmi. Then, the obtained PDAmi/$Ti_3C_2T_x$ composites were calcined at 350 °C (**Figure 1d**) under N_2 atmosphere to remove the block copolymer (**Figure S4**) and, at the same time, to oxidize the PDA molecules to form more quinone groups.[24] As seen in **Figure 2d-e** and **S5a-c**, the bumps disappeared and ordered mesoporous PDA is deposited on the $Ti_3C_2T_x$ surface after calcination. The average pore size is ~20 nm, which is slightly smaller than the average diameter of the bumps. The cross-sectional TEM images clearly show the sandwich structure of OMPDA/$Ti_3C_2T_x$ composites (**Figure 2f** and **Figure S5d**). The thickness of the PDA coating on the two sides of $Ti_3C_2T_x$ is estimated to be ~14 nm, which slightly differs from the thickness prior to the heat-treatment process. The shrinkage of the PDA layers is be attributed to the thermal treatment process. From **Figure S6**, it is evident that the mesoporous OMPDA is uniformly deposited on the $Ti_3C_2T_x$ surface.

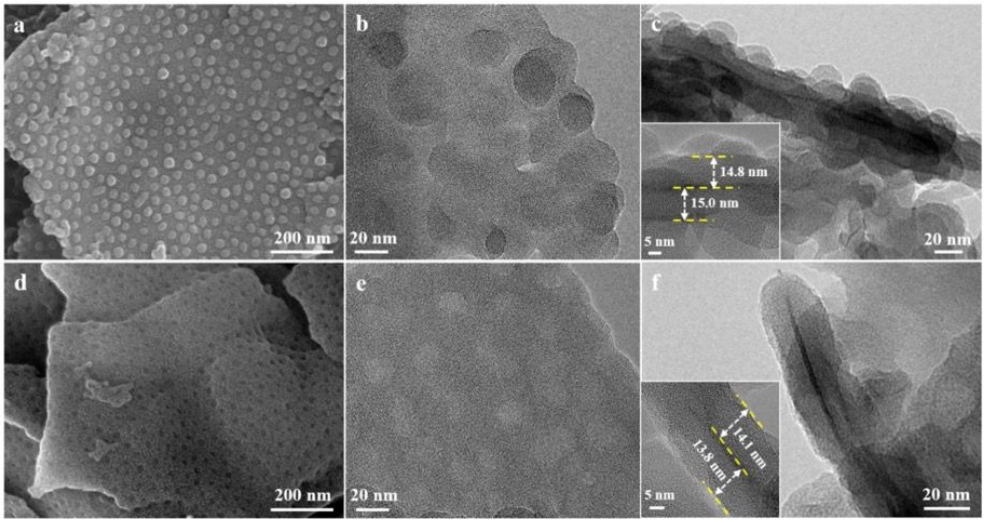

Figure 2. (a) SEM and (b-c) TEM images of PDAmi/$Ti_3C_2T_x$. (d) SEM and (e-f) TEM images of OMPDA/$Ti_3C_2T_x$.

To investigate the factors which influence the mesoporous structure of PDA layer, a series of OMPDA/$Ti_3C_2T_x$ samples were prepared with different ratios of dopamine and $Ti_3C_2T_x$. In the absence of PS-*b*-PEO, PDA/$Ti_3C_2T_x$ sheets without bumps are obtained after polymerization (**Figure S7a**). After heat treatment, the smooth surface is retained for SPDA/$Ti_3C_2T_x$ (**Figure S7b-e**), indicating the vital role of PS-*b*-PEO in the formation of micelles and mesopores after the heat treatment process. Without adding $Ti_3C_2T_x$, PDAmi spheres of ~210 nm with coarse surfaces are obtained (**Figure S8a-b**), which leads to ordered mesoporous PDA (OMPDA) spheres after heat

treatment (**Figure S8c-d**). By decreasing the amount of $Ti_3C_2T_x$ from 50 to 25 mg, the density of micelles on the surface of $Ti_3C_2T_x$ is increased and aggregation of particles is observed outside the nanosheets (**Figure S9a-b**). On the contrary, by increasing the amount of $Ti_3C_2T_x$ to 75 mg, the amount of the bumps on the surface of $Ti_3C_2T_x$ is reduced (**Figure S9c**). After heating, the mesopores are not very obvious (**Figure S9d**), which may be attributed to the small thickness of the PDA layer. These observations indicate that the proportion of DAmi affects the density of bumps on the $Ti_3C_2T_x$ surface (**Figure S10**). The formation process can be deduced as follows. After the addition of the ammonia solution, the polymerization takes place surrounding DAmi. After heat treatment, mesopores are generated by the elimination of the PS-*b*-PEO template. However, the mesoporous structure is not so evident for the composite containing an excessive $Ti_3C_2T_x$ phase (75 mg). It is observed that the OMPDA/$Ti_3C_2T_x$ composite prepared with 50 mg of $Ti_3C_2T_x$ displays the most homogeneous sandwich structure and hence, and we have chosen this particular sample for further investigations. The specific surface area (SSA) of the typical OMPDA/$Ti_3C_2T_x$ sample prepared with 50 mg is discussed later, but the SSAs of OMPDA/$Ti_3C_2T_x$-25 (85.5 m^2 g^{-1}) and OMPDA/$Ti_3C_2T_x$-75 (43.3 m^2 g^{-1}) are much lower than the typical OMPDA/$Ti_3C_2T_x$ sample (129.2 m^2 g^{-1}).

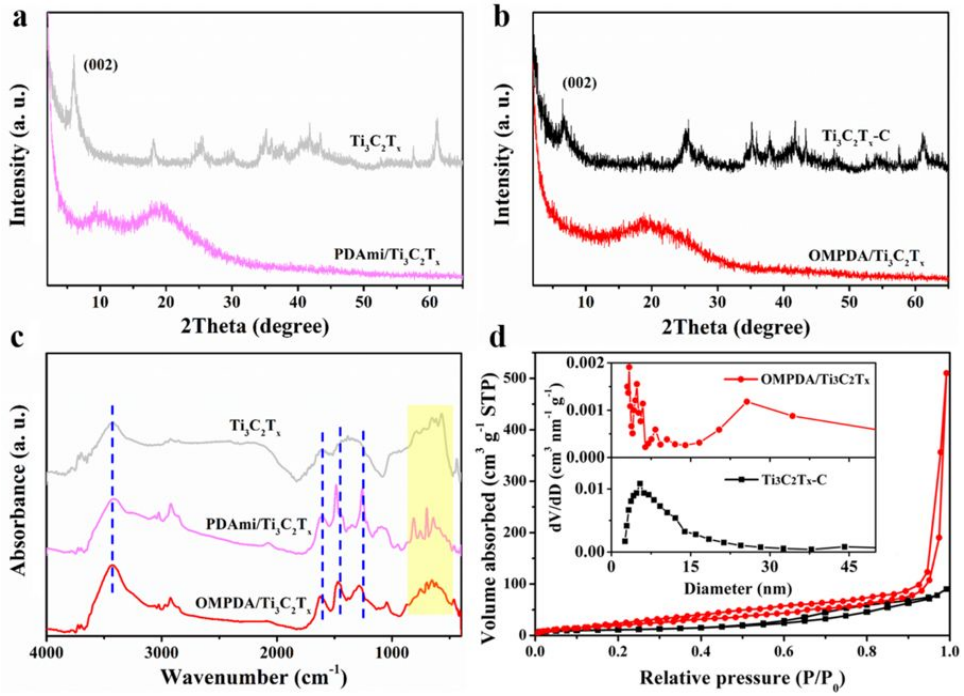

Figure 3. (a) Wide-angle XRD patterns of $Ti_3C_2T_x$ and PDAmi/$Ti_3C_2T_x$. (b) Wide-angle XRD patterns of $Ti_3C_2T_x$ after heat-treatment ($Ti_3C_2T_x$-C) and OMPDA/$Ti_3C_2T_x$. (c) FT-IR spectra of $Ti_3C_2T_x$, PDAmi/$Ti_3C_2T_x$, and OMPDA/$Ti_3C_2T_x$. (d) Nitrogen sorption isotherms of $Ti_3C_2T_x$-C and OMPDA/$Ti_3C_2T_x$ (insets: pore size distribution curves).

X-ray diffraction (XRD) measurements were performed to determine the compositional differences between $Ti_3C_2T_x$, PDAmi/$Ti_3C_2T_x$, and OMPDA/$Ti_3C_2T_x$ composites (**Figure 3a-b**). The XRD pattern of pure $Ti_3C_2T_x$ shows a (002) peak at 2θ = 6.0°, corresponding to the typical layered structure of MXene.[26,42-43] The *d*-spacing between $Ti_3C_2T_x$ layers is calculated to be 1.47 nm. After coating with PDAmi, the (002) peak disappears. The XRD pattern of PDA/$Ti_3C_2T_x$ exhibits a (002) peak at 2θ = 4.5° (**Figure S11a**), corresponding to an increased *d*-spacing of 1.96 nm. In addition, in the XRD pattern of the physical mixture of PDAmi spheres and $Ti_3C_2T_x$ (PDAmi-$Ti_3C_2T_x$ mixture), a (002) peak at 2θ = 6.0° is observed (**Figure S11a**), indicating that the *d*-spacing between $Ti_3C_2T_x$ layers is unchanged, compared with the original $Ti_3C_2T_x$ material. This indicates that the existence of micelles can effectively prevent the stacking of $Ti_3C_2T_x$ nanosheets, thus leading to the disappearance of (002) peak. **Figure 3b** and **Figure S11b** show the XRD patterns after the heat treatment at 350 °C.

To confirm the successful coating of PDA on the $Ti_3C_2T_x$ surface, Fourier transform-infrared spectroscopy (FT-IR) analysis was conducted and the results are presented in **Figure 3c** and **Figure S12a**. The IR peaks at 3420, 1620, 1480 and 1260 cm^{-1} correspond to an asymmetric stretch of –OH, bending vibration of –OH, bending vibration of indole-indoline, and scissoring vibration of CH_2, respectively.[43] The peaks at around 1480 and 1260 cm^{-1} show an obvious increase for the PDAmi/$Ti_3C_2T_x$ composites, suggesting the interaction between catechols/quinone groups in dopamine molecules and –OH/–F terminal groups of $Ti_3C_2T_x$. The peak at around 700 cm^{-1} can be attributed to PS-*b*-PEO. The structural analysis of PDA, including the molecular weight and polydispersity, is challenging because PDA is difficult to dissolve in water and organic solvents.[44-46] For comparison, we have also prepared PDA under the same conditions but in the absence of $Ti_3C_2T_x$. Compared with the DA precursor,[47] the peak observed at 3500 cm^{-1} is shifted to 3300 cm^{-1} in PDA (**Figure S12b**), indicating the disappearance of the asymmetric stretching of H–N–H group. These results suggest the successful coverage of $Ti_3C_2T_x$ by PDA. In the spectrum of OMPDA/$Ti_3C_2T_x$, the peaks at around 1620, 1480 and 1260 cm^{-1} remain more or less similar with a little decrease in peak intensity, suggesting the well-retained structure of PDA. The peak at 700 cm^{-1} disappears, suggesting the successful removal of the block copolymer template. The weight percentage of $Ti_3C_2T_x$ in the OMPDA/$Ti_3C_2T_x$ composite is ~41 % based on the thermogravimetric (TG) measurement carried out in the air (**Figure S13**).

The porous structures of $Ti_3C_2T_x$-C, OMPDA/$Ti_3C_2T_x$, and SPDA/$Ti_3C_2T_x$ were analyzed by nitrogen sorption measurements (**Figure 3d** and **Figure S14**). OMPDA/$Ti_3C_2T_x$ shows an isotherm with a small hysteresis loop (**Figure 3d**), suggesting the porous nature.[48] The pore size distribution

curve of OMPDA/$Ti_3C_2T_x$ shows one broad peak at *ca*. 25 nm (**Figure 3d inset**), which originates from the mesopores of OMPDA. The surface area of OMPDA/$Ti_3C_2T_x$ is ~129 m^2 g^{-1}, which is superior to those of SPDA/$Ti_3C_2T_x$ (59 m^2 g^{-1}) and $Ti_3C_2T_x$-C (39 m^2 g^{-1}). $Ti_3C_2T_x$-C shows the presence of small-sized pores with around 5 nm (*i.e.*, interlayer space) which is formed by the re-stacking of $Ti_3C_2T_x$ nanosheets,[43,49] while SPDA/$Ti_3C_2T_x$ exhibits no porosity because the interlayer space is seriously blocked by PDA.

Electrochemical performance

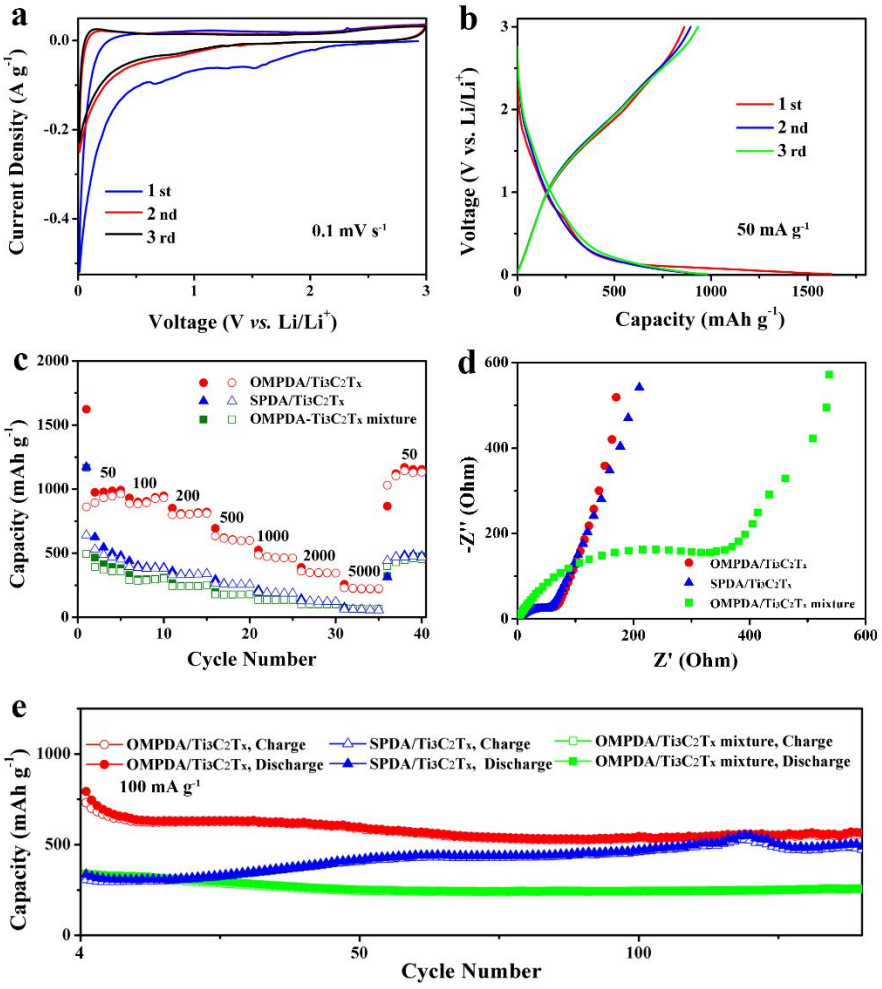

Figure 4. (a) CV and (b) charge-discharge curves of OMPDA/$Ti_3C_2T_x$ electrode in the voltage window from 0.01 V to 3.0 V. (c) Rate capability at various current densities, (d) Nyquist plots, and (e) cycling stability of OMPDA/$Ti_3C_2T_x$, SPDA/$Ti_3C_2T_x$, and OMPDA-$Ti_3C_2T_x$ electrodes after three charge-discharge cycles.

The electrochemical performance of the OMPDA/$Ti_3C_2T_x$ sample is initially assessed by the cyclic voltammetry (CV) technique using a half-cell configuration. In the first cathodic sweep of the

CV curves of OMPDA/$Ti_3C_2T_x$ (**Figure 4a**), the peaks at ~1.5 V and 0.67 V correspond to the addition of lithium to unsaturated nitrogen and the enolization reaction of lithium with carbonyl oxygen.[27,28] The pronounced broad peak seen below 0.4 V is indexed to the intercalation of Li^+ into C_6 aromatic rings and the generation of the SEI film at the interface between electrode and electrolyte.[27,28] The following second and third CV curves almost overlap. This indicates that the redox properties of OMPDA/$Ti_3C_2T_x$ are largely reversible. The discharge-charge profiles of the OMPDA/$Ti_3C_2T_x$ electrode shown in **Figure 4b** display the same trend as that observed in the CV results. During the discharge process (Li^+ intercalation), the curves show a fast decrease in capacity from 2.8 to 0.4 V and then a slow decline to 0.01 V. Then, an inclined curve is seen during the charging process (Li^+ de-intercalation). The similar shapes of the discharge-charge curves of OMPDA/$Ti_3C_2T_x$, SPDA/$Ti_3C_2T_x$, and OMPDA-$Ti_3C_2T_x$ mixture at 100 mA g^{-1} (**Figure S15**) reveal a similar energy storage mechanism of PDA materials. **Figure 4c** compares the capacities of OMPDA/$Ti_3C_2T_x$, SPDA/$Ti_3C_2T_x$, and OMPDA-$Ti_3C_2T_x$ mixture electrodes at various current densities (50~5000 mAh g^{-1}). At a current density of 50 mA g^{-1}, the OMPDA/$Ti_3C_2T_x$ electrode shows initial specific discharge and charge capacities of are 1623 and 862 mAh g^{-1}, respectively, with a Coulombic efficiency of 53%. The low Coulombic efficiency in the initial cycle is mostly attributed to the generation of an SEI film, which an irreversible process. In the subsequent cycle, the Coulombic efficiency is enhanced to 92% and reaches over 95% starting from the third cycle. The capacity of the OMPDA/$Ti_3C_2T_x$ electrode reaches up to ~1000 mAh g^{-1}. Compared to OMPDA/$Ti_3C_2T_x$, the SPDA/$Ti_3C_2T_x$ electrode shows a much lower capacity (~500 mAh g^{-1}) and Coulombic efficiency. These results suggest that the existence of mesopores on PDA can enhance the overall capacity and reversibility of the reactions with lithium ions. With increasing current density, the capacity of the OMPDA/$Ti_3C_2T_x$ electrode decreases much more slowly than those of SPDA/$Ti_3C_2T_x$ and OMPDA-$Ti_3C_2T_x$ mixture electrodes. The OMPDA/$Ti_3C_2T_x$ electrode retains capacity of ~230 mAh g^{-1} at 5000 mA g^{-1}. In comparison, the capacities of SPDA/$Ti_3C_2T_x$ and OMPDA-$Ti_3C_2T_x$ mixture electrodes at the same rate decrease to ~65 and ~60 mAh g^{-1}, respectively. The performance of OMPDA/$Ti_3C_2T_x$ is also better than many previously reported polymer-based electrodes (**Table S1**). It is noted that the capacitance of OMPDA/$Ti_3C_2T_x$ is similar to that of pure PDA.[24,26] Considering the low capacitance of pure $Ti_3C_2T_x$ (~100 mAh g^{-1}), the capacitance contribution from OMPDA to the capacitance of the OMPDA/$Ti_3C_2T_x$ composite is supposed to be much higher compared to pure PDA. The high capacity and excellent rate capability of the OMPDA/$Ti_3C_2T_x$ may originate from the heterostructure of OMPDA and $Ti_3C_2T_x$. Electrochemical impedance spectroscopy (EIS) measurements were carried out to investigate the electrode kinetics. From **Figure 4d**, it can be observed that, among the three electrodes, OMPDA/$Ti_3C_2T_x$ shows the

least charge transfer resistance (R_{ct}), which further confirms the important roles of the mesopores. The mesoporous structure increases the specific surface area, leading to a high capacity, and reduces the areal current density, resulting in lower electrode polarization. The mesopores also promote better infiltration of the electrolyte ions into the active material by shortening the length for ion diffusion. Therefore, the construction of mesopores in the polymers combined with the use of highly conductive substrates provides an effective strategy for designing high-performance electrodes based on organic polymers. **Figure 4e** and **Figure S16** display the cycling stability of OMPDA/$Ti_3C_2T_x$, SPDA/$Ti_3C_2T_x$, and OMPDA-$Ti_3C_2T_x$ composite electrodes at 100 mA g^{-1} and 1000 mA g^{-1}, respectively. At 1000 mA g^{-1}, during the initial 80 cycles, the capacity of OMPDA/$Ti_3C_2T_x$ slowly rises to ~430 mAh g^{-1} and remains constant in subsequent cycles, while the Coulombic efficiency is stable at 100% during cycling. For the SPDA/$Ti_3C_2T_x$ electrode, the capacity increases from 122 mAh g^{-1} to 346 mAh g^{-1} after 200 cycles, and then gradually decreases to 170 mAh g^{-1}. The capacity of the OMPDA-$Ti_3C_2T_x$ mixture electrode starts to decrease after 50 cycles, before finally dropping to 135 mAh g^{-1}. These findings indicate that combining PDA with $Ti_3C_2T_x$ can improve the structural stability of OMPDA.

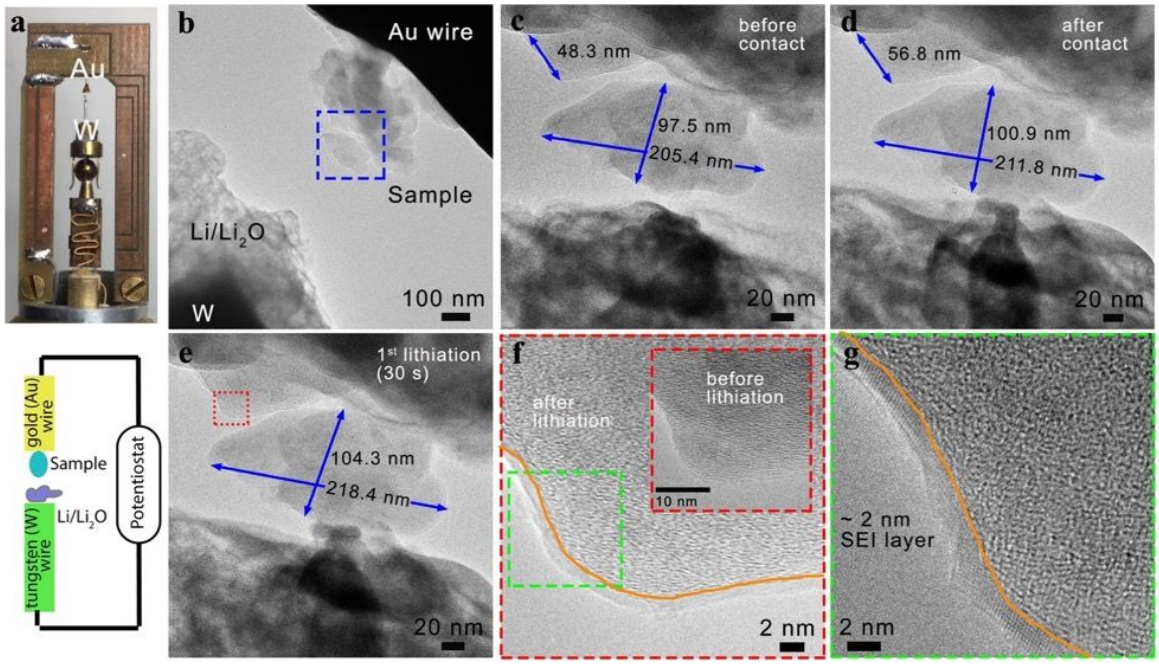

Figure 5. (a) Digital photo and schematic drawing of the *in situ* TEM experiment. (b) Low magnification TEM picture of OMPDA/$Ti_3C_2T_x$ composite prior to the contact with the Li/Li_2O electrode. (c) Magnified TEM picture of the boxed area in Figure 5b. (d) The TEM image of the OMPDA/$Ti_3C_2T_x$ sample, soon after coming into contact with the Li/Li_2O electrode before applying a bias. (e) TEM picture was taken at 30 s point during the 1st lithiation (*i.e.*, after applying a bias of –3 V). (f) Magnified TEM picture of the boxed area in Figure 5e (inset shows the TEM image of the

same region before coming into contact with Li/Li_2O electrode). (g) Magnified TEM picture of the boxed area (green) in Figure 5f.

To investigate the mechanisms behind the excellent performance of OMPDA/$Ti_3C_2T_x$, real-time *in situ* TEM observation was performed to visualize the changes in morphology, structure, and volume of OMPDA/$Ti_3C_2T_x$ during (de)lithiation. The digital photo of the *in situ* TEM setup with a schematic illustration is depicted in **Figure 5a**. The TEM image reveals that the freestanding OMPDA/$Ti_3C_2T_x$ sample is fixed on an Au wire (**Figure 5b**), while a layer of Li/Li_2O is set on a movable W probe of scanning tunneling TEM (STM-TEM) holder. **Figure 5c** shows the magnified region of OMPDA/$Ti_3C_2T_x$ (the area inside the blue box in **Figure 5b**) which is visualized and recorded under TEM during (de)lithiation. Interestingly, there is a small volume expansion of OMPDA/$Ti_3C_2T_x$ along with all directions soon after contact with Li/Li_2O (*i.e.*, before the application of bias), indicating effective Li uptake by the novel OMPDA/$Ti_3C_2T_x$ material (compare to **Figures 5c-d**). At a potential of –3 V *versus* Li/Li^+, a further volume expansion of the material is observed; changes in distances from 211.8 to 218.4 nm and from 100.9 to 104.3 nm along horizontal and vertical directions are observed, respectively, which accounts for a volume expansion of ~20 % with respect to the initial state (**Figure 5e**, **Movie S1**). In the nano-battery device, the layer of Li_2O formed on the Li electrode during specimen holder insertion can serve as a solid electrolyte. In **Figure 5f**, we present an area of the material which has not been in direct contact with the Li/Li_2O electrode (area marked by a red box in **Figure 5e**) after lithiation. We also observe that a thin outer membrane is formed on OMPDA/$Ti_3C_2T_x$ material surface, which is likely the SEI layer formed in conventional electrochemical cells. The thickness of this layer after the first lithiation is ~2 nm (**Figure 5g**). A separate *in situ* (de)lithiation experiment (**Figure S17**) shows that the thickness of the SEI layer remains unchanged after two (de)lithiation cycles. Even after applying a high voltage (–6 V *versus* Li/Li^+), the SEI layer remains stable during the (de)lithiation process. Thus, *in situ* TEM experiments reveal that the distinctive morphology of OMPDA/$Ti_3C_2T_x$ promotes the formation of an ultrathin and stable SEI membrane outside the material surface. This SEI layer can act as a "surface-passivating film" which creates a barrier for electrolyte penetration and prevents SEI formation inside the active material, hence improving the electrochemical stability during cycling.[50] It should be noted here that apart from minor volume expansion in the 1st lithiation, there is no obvious structural change to the material during (de)lithiation. Therefore, the OMPDA/$Ti_3C_2T_x$ composite only shows minor volume expansion during cycling due to its excellent structural integrity.

Conclusions

In conclusion, we have developed a sandwich-structured OMPDA/$Ti_3C_2T_x$ composite through *in situ* assembly of DA-PS-*b*-PEO micelles on the highly conductive $Ti_3C_2T_x$ substrate, followed by polymerization and subsequent heat treatment. Owing to the vertically-oriented mesopores on the surface and the combination with $Ti_3C_2T_x$, the as-prepared OMPDA/$Ti_3C_2T_x$ composite shows significantly enhanced lithium storage compared to common polymer-based electrodes. The OMPDA/$Ti_3C_2T_x$ composite electrode delivers a high reversible capacity (~1000 mAh g^{-1} at 50 mA g^{-1}) along with long stability and good rate capability. The presented work offers an effective strategy to rationally design and fabricate polymer-based electrodes with high-performance for rechargeable batteries.

METHODS

Chemicals: Dopamine hydrochloride (DA), ammonia solution (25-28 wt.%), ethanol, and tetrahydrofuran (THF) were purchased from Sigma-Aldrich. PS-*b*-PEO was obtained from Polymer Source Inc.

Preparation of $Ti_3C_2T_x$: The exfoliated $Ti_3C_2T_x$ nanosheets were synthesized according to an established method.[45] Then, a solution of $Ti_3C_2T_x$ was made by dissolving 1 g of $Ti_3C_2T_x$ in 10 mL of deionized water for further use.

Preparation of polydopamine-PS-b-PEO micelles (PDAmi)/$Ti_3C_2T_x$ composite: First, 600 mg of DA was dispersed in a mixture solution consisting of deionized water (16 mL) and ethanol (8 mL). After that, 8 mL of THF solution, which contained 60 mg of PS-*b*-PEO, was added and the resulting mixture solution was stirred for 1 h under ambient conditions. Afterward, 8 mL of $Ti_3C_2T_x$ aqueous solution (1 g/10 mL) was added. After stirring for another 2 h, 1 mL of ammonia solution was dropped into the mixture solution. Upon further stirring at room temperature (RT) under nitrogen flow for 20 h, the PDAmi/$Ti_3C_2T_x$ composite was obtained by filtration and subsequently washed with ethanol and deionized water. By changing the amount of $Ti_3C_2T_x$ to 25 mg and 75 mg, the samples, PDAmi/$Ti_3C_2T_x$-25 and PDAmi/$Ti_3C_2T_x$-75, respectively, were obtained.

Preparation of ordered mesoporous PDA (OMPDA)/$Ti_3C_2T_x$ composite: The as-obtained PDAmi/$Ti_3C_2T_x$ composite was calcined under N_2 flow at 350 ^oC for 10 h (ramping rate: 2 ^oC min^{-1}), leading to the attainment of a sandwich-structured OMPDA/$Ti_3C_2T_x$. By calcining PDAmi/$Ti_3C_2T_x$-25 and PDAmi/$Ti_3C_2T_x$-75 under the same heating conditions, the samples, OMPDA/$Ti_3C_2T_x$-25 and OMPDA/$Ti_3C_2T_x$-75, respectively, were achieved.

Preparation of smooth PDA (SPDA)/$Ti_3C_2T_x$ composite: The preparation steps for the PDA/$Ti_3C_2T_x$ composite were similar to those of PDAmi/$Ti_3C_2T_x$ but without using THF solution of PS-*b*-PEO in the initial step. The material obtained after calcination is referred to as SPDA/$Ti_3C_2T_x$.

Preparation of $Ti_3C_2T_x$ after heat treatment ($Ti_3C_2T_x$-C): The $Ti_3C_2T_x$-C sample was obtained through pyrolysis of $Ti_3C_2T_x$ under N_2 flow at 350 ^oC for 10 h (ramping rate: 2 ^oC min^{-1}).

Preparation of OMPDA spheres: 600 mg of DA was dissolved in a mixture solution composed of deionized water (16 mL) and ethanol (8 mL). After that, 8 mL of THF solution, which contained 60 mg of PS-*b*-PEO, was added and stirred for 1 h under ambient conditions. Then, 1 mL of ammonia solution was added into the solution. Upon further stirring at RT for 20 h, the PDAmi spheres were obtained by filtration and subsequently washing with ethanol and deionized water. After calcination at 350 ^oC under N_2 atmosphere for 10 h, OMPDA spheres were obtained.

Characterization: Field-emission scanning electron microscopy (FESEM) observations were taken on a Hitachi S-4800 microscope. Transmission electron microscopy (TEM) observations with energy-dispersive X-ray (EDX) analysis were performed on a JEOL JEM-2100 at 200 kV. The phase compositions of the samples were analyzed using a Rigaku Rint 2000 X-ray diffractometer with monochromated Cu Kα radiation. Fourier transform infrared (FT-IR) spectra were obtained using the Thermoscientific Nicolet 4700 FT-IR Spectroscopy. Thermogravimetric (TG) measurements were conducted on a Hitachi HT-Seiko Instrument Exter 6300 TG/DTA. Nitrogen sorption measurements were conducted using AUTOSORB-1. The specific surface area (SSA) was calculated by employing the Brunauer-Emmett-Teller (BET) theory at a relative pressure range of 0.05-0.30. The pore size distribution was analyzed using the adsorption data of the isotherm with the Barrett-Joyner-Halenda (BJH) model.

Electrochemical Measurements: The working electrode was made by mixing the active material, acetylene black, and carboxymethyl cellulose binder (weight ratio is 7:2:1) and then coated onto a current collector (copper foil). After drying, the electrode was cut into disks. The CR-2016-type coin cell was fabricated in a glovebox, by using 1 M $LiPF_6$ in ethylene carbonate (EC)/diethyl carbonate (DMC) (1:1, *w/w*) as the electrolyte and lithium foil as the counter electrode. Cyclic voltammetry (CV) and electrochemical impedance spectroscopy (EIS) measurements were conducted using an electrochemical workstation (CHI 660E). Galvanostatic charge-discharge measurements were tested using a Land CT2001A battery testing system at ambient conditions.

SUPPORTING INFORMATION

SEM, TEM, and STEM images with elemental mapping, TEM images, TGA curves, XRD patterns, FT-IR spectra, GCD curves, cycling performance, and schematic drawing of the formation mechanism are supplied as Supporting information.

ACKNOWLEDGMENTS

The authors gratefully acknowledge the financial support from Australian Research Council (ARC) Future Fellow (Grant FT150100479), ARC Linkage (LP180100429), Natural Science Foundation of Jiangsu Province (No. BK20170778), and NSFC (No. 51672128, 21773118, U1802256). T.L. acknowledges the funding provided by the Fundamental Research Funds for the Central Universities (CUSF–DH–D–2018001) and the China Scholarship Council (201806630044). J.W. and B.D. thank the Japan Society for the Promotion of Science (JSPS) for providing the JSPS Fellowships (18F18038, 18F18764). This work was partly conducted at the Queensland node of the Australian National Fabrication Facility Queensland Node (ANFF-Q), a company established under the National Collaborative Research Infrastructure Strategy to provide nano- and micro-fabrication facilities for Australian researchers.

References

(1) Li, M.; Lu, J.; Chen, Z.; Amine, K.: 30 Years of Lithium-Ion Batteries. *Adv. Mater.* **2018**, *30*, 1800561.

(2) Winter, M.; Barnett, B.; Xu, K.: Before Li Ion Batteries. *Chem. Rev.* **2018**, *118*, 11433-11456.

(3) Cao, Y.; Li, M.; Lu, J.; Liu, J.; Amine, K.: Bridging the Academic and Industrial Metrics for Next-Generation Practical Batteries. *Nat. Nanotechnol.* **2019**, *14*, 200-207.

(4) Susai, F. A.; Sclar, H.; Shilina, Y.; Penki, T. R.; Raman, R.; Maddukuri, S.; Maiti, S.; Halalay, I. C.; Luski, S.; Markovsky, B.; Aurbach, D.: Horizons for Li-Ion Batteries Relevant to Electro-Mobility: High-Specific-Energy Cathodes and Chemically Active Separators. *Adv. Mater.* **2018**, *30*, 1801348.

(5) Zhu, C.; Usiskin, R. E.; Yu, Y.; Maier, J.: The Nanoscale Circuitry of Battery Electrodes. *Science* **2017**, *358*, eaao2808.

(6) Kim, T.; Song, W.; Son, D.-Y.; Ono, L. K.; Qi, Y.: Lithium-ion Batteries: Outlook on Present, Future, and Hybridized Technologies. *J. Mater. Chem. A* **2019**, *7*, 2942-2964.

(7) Wang, J.; Kim, J.; Ding, B.; Kim, J. H.; Malgras, V.; Young, C.; Yamauchi, Y. Ultra-Thin, Highly Graphitized Carbon Nanosheets into Three-Dimensional Interconnected Framework Utilizing A Ball Mill Mixing of Precursors. *Chem. Eng. J.* **2019**, *374*, 1214-1220.

(8) Zhu, G. L.; Zhao, C. Z.; Huang, J. Q.; He, C.; Zhang, J.; Chen, S.; Xu, L.; Yuan, H.; Zhang, Q.: Fast Charging Lithium Batteries: Recent Progress and Future Prospects. *Small* **2019**, *15*, 1805389.

(9) Lu, Y.; Yu, L.; Lou, X. W.: Nanostructured Conversion-type Anode Materials for Advanced Lithium-Ion Batteries. *Chem* **2018**, *4*, 972-996.

(10) Peterson, B. M.; Ren, D.; Shen, L.; Wu, Y.-C. M.; Ulgut, B.; Coates, G. W.; Abruña, H. D.; Fors, B. P.: Phenothiazine-Based Polymer Cathode Materials with Ultrahigh Power Densities for Lithium Ion Batteries. *ACS Appl. Energy Mater.* **2018**, *1*, 3560-3564.

(11) Sun, Y.; Liu, N.; Cui, Y.: Promises and Challenges of Nanomaterials for Lithium-based Rechargeable Batteries. *Nat. Energy* **2016**, *1*, 16071.

(12) Luo, C.; Borodin, O.; Ji, X.; Hou, S.; Gaskell, K. J.; Fan, X.; Chen, J.; Deng, T.; Wang, R.; Jiang, J.; Wang, C.: Azo Compounds as a Family of Organic Electrode Materials for Alkali-ion Batteries. *Proc. Natl. Acad. Sci.* **2018**, *115*, 2004-2009.

(13) Liang, Y.; Tao, Z.; Chen, J.: Organic Electrode Materials for Rechargeable Lithium Batteries. *Adv. Energy Mater.* **2012**, *2*, 742-769.

(14) Peng, C.; Ning, G.-H.; Su, J.; Zhong, G.; Tang, W.; Tian, B.; Su, C.; Yu, D.; Zu, L.; Yang, J.; Ng, M.-F.; Hu, Y.-S.; Yang, Y.; Armand, M.; Loh, K. P.: Reversible Multi-electron Redox Chemistry of π-conjugated N-containing Heteroaromatic Molecule-based Organic Cathodes. *Nat. Energy* **2017**, *2*, 17074.

(15) Lee, S.; Kwon, G.; Ku, K.; Yoon, K.; Jung, S. K.; Lim, H. D.; Kang, K.: Recent Progress in Organic Electrodes for Li and Na Rechargeable Batteries. *Adv. Mater.* **2018**, *30*, 1704682.

(16) Liang, Y.; Jing, Y.; Gheytani, S.; Lee, K. Y.; Liu, P.; Facchetti, A.; Yao, Y.: Universal Quinone Electrodes for Long Cycle Life Aqueous Rechargeable Batteries. *Nat. Mater.* **2017**, *16*, 841-848.

(17) Bhosale, M. E.; Chae, S.; Kim, J. M.; Choi, J.-Y.: Organic Small Molecules and Polymers as An Electrode Material for Rechargeable Lithium Ion Batteries. *J. Mater. Chem. A* **2018**, *6*, 19885-19911.

(18) Luo, Z.; Liu, L.; Zhao, Q.; Li, F.; Chen, J.: An Insoluble Benzoquinone-Based Organic Cathode for Use in Rechargeable Lithium-Ion Batteries. *Angew. Chem. Int. Ed.* **2017**, *56*, 12561-12565.

(19) J. R. Dahn, T. Z., Yinghu Liu, J. S. Xue: Mechanisms for Lithium Insertion In Carbonaceous Materials. *Science* **1995**, *270*, 590-593.

(20) Häupler, B.; Wild, A.; Schubert, U. S.: Carbonyls: Powerful Organic Materials for Secondary Batteries. *Adv. Energy Mater.* **2015**, *5*, 1402034.

(21) Fédèle, L.; Sauvage, F.; Gottis, S.; Davoisne, C.; Salager, E.; Chotard, J.-N.; Becuwe, M.: 2D-Layered Lithium Carboxylate Based on Biphenyl Core as Negative Electrode for Organic Lithium-Ion Batteries. *Chem. Mater.* **2017**, *29*, 546-554.

(22) Jouhara, A.; Dupre, N.; Gaillot, A. C.; Guyomard, D.; Dolhem, F.; Poizot, P.: Raising the Redox Potential in Carboxyphenolate-based Positive Organic Materials via Cation Substitution. *Nat. Commun.* **2018**, *9*, 4401.

(23) Armand, M.; Grugeon, S.; Vezin, H.; Laruelle, S.; Ribiere, P.; Poizot, P.; Tarascon, J. M.: Conjugated Dicarboxylate Anodes for Li-ion Batteries. *Nat. Mater.* **2009**, *8*, 120-125.

(24) Sun, T.; Li, Z.-J.; Wang, H.-G.; Bao, D.; Meng, F.-L.; Zhang, X.-B.: A Biodegradable Polydopamine-Derived Electrode Material for High-Capacity and Long-Life Lithium-Ion and Sodium-Ion Batteries. *Angew. Chem. Int. Ed.* **2016**, *55*, 10662-10666.

(25) Qu, K.; Wang, Y.; Vasileff, A.; Jiao, Y.; Chen, H.; Zheng, Y.: Polydopamine-inspired Nanomaterials for Energy Conversion and Storage. *J. Mater. Chem. A* **2018**, *6*, 21827-21846.

(26) Dong, X.; Ding, B.; Guo, H.; Dou, H.; Zhang, X.: Superlithiated Polydopamine Derivative for High-Capacity and High-Rate Anode for Lithium-Ion Batteries. *ACS Appl. Mater. Interfaces* ***2018****, 10, 38101-38108.*

(27) Zhou, H.; Zhang, R.; Song, S.; Xiao, C.; Gao, G.; Ding, S.: Dopamine-Assisted Synthesis of MoS_2 Nanosheets on Carbon Nanotube for Improved Lithium and Sodium Storage Properties. *ACS Appl. Energy Mater.* **2018**, *1*, 5112-5118.

(28) Gueon, D.; Moon, J. H.: Polydopamine-wrapped, Silicon Nanoparticle-impregnated Macroporous CNT Particles: Rational Design of High-performance Lithium-ion Battery Anodes. *Chem. Commun.* **2019**, *55*, 361-364.

(29) Liu, T.; Kim, K. C.; Lee, B.; Chen, Z.; Noda, S.; Jang, S. S.; Lee, S. W.: Self-polymerized Dopamine as An Organic Cathode for Li- and Na-ion Batteries. *Energy Environ. Sci.* **2017**, *10*, 205-215.

(30) Amin, K.; Meng, Q.; Ahmad, A.; Cheng, M.; Zhang, M.; Mao, L.; Lu, K.; Wei, Z.: A Carbonyl Compound-Based Flexible Cathode with Superior Rate Performance and Cyclic Stability for Flexible Lithium-Ion Batteries. *Adv. Mater.* **2018**, *30*, 1703868.

(31) Fang, R.; Chen, K.; Yin, L.; Sun, Z.; Li, F.; Cheng, H. M.: The Regulating Role of Carbon Nanotubes and Graphene in Lithium-Ion and Lithium-Sulfur Batteries. *Adv. Mater.* **2019**, *31*, 1800863.

(32) Kwon, Y. H.; Minnici, K.; Park, J. J.; Lee, S. R.; Zhang, G.; Takeuchi, E. S.; Takeuchi, K. J.; Marschilok, A. C.; Reichmanis, E.: SWNT Anchored with Carboxylated Polythiophene "Links" on High-Capacity Li-Ion Battery Anode Materials. *J. Am. Chem. Soc.* **2018**, *140*, 5666-5669.

(33) Zhou, L.; Zhang, K.; Hu, Z.; Tao, Z.; Mai, L.; Kang, Y.-M.; Chou, S.-L.; Chen, J.: Recent Developments on and Prospects for Electrode Materials with Hierarchical Structures for Lithium-Ion Batteries. *Adv. Energy Mater.* **2018**, *8*, 1701415.

(34) Gu, D.; Li, W.; Wang, F.; Bongard, H.; Spliethoff, B.; Schmidt, W.; Weidenthaler, C.; Xia, Y.; Zhao, D.; Schuth, F.: Controllable Synthesis of Mesoporous Peapod-like Co_3O_4@Carbon Nanotube Arrays for High-Performance Lithium-Ion Batteries. *Angew. Chem. Int. Ed.* **2015**, *54*, 7060-7064.

(35) Fang, Y.; Lv, Y.; Gong, F.; Elzatahry, A. A.; Zheng, G.; Zhao, D.: Synthesis of 2D-Mesoporous-Carbon/MoS_2 Heterostructures with Well-Defined Interfaces for High-Performance Lithium-Ion Batteries. *Adv. Mater.* **2016**, *28*, 9385-9390.

(36) Fang, Y.; Lv, Y.; Che, R.; Wu, H.; Zhang, X.; Gu, D.; Zheng, G.; Zhao, D.: Two-dimensional Mesoporous Carbon Nanosheets and Their Derived Graphene Nanosheets: Synthesis and Efficient Lithium Ion Storage. *J. Am. Chem. Soc.* **2013**, *135*, 1524-1530.

(37) Lan, K.; Liu, Y.; Zhang, W.; Liu, Y.; Elzatahry, A.; Wang, R.; Xia, Y.; Al-Dhayan, D.; Zheng, N.; Zhao, D.: Uniform Ordered Two-Dimensional Mesoporous TiO_2 Nanosheets from Hydrothermal-Induced Solvent-Confined Monomicelle Assembly. *J. Am. Chem. Soc.* 2018, 140, 4135-4143.

(38) Anasori, B.; Lukatskaya, M. R.; Gogotsi, Y.: 2D Metal Carbides and Nitrides (MXenes) for Energy Storage. *Nat. Rev. Mater.* **2017**, *2*, 16098.

(39) Niu, S.; Wang, Z.; Yu, M.; Yu, M.; Xiu, L.; Wang, S.; Wu, X.; Qiu, J.: MXene-Based Electrode with Enhanced Pseudocapacitance and Volumetric Capacity for Power-Type and Ultra-Long Life Lithium Storage. *ACS Nano* **2018**, *12*, 3928-3937.

(40) Tang, J.; Liu, J.; Li, C.; Li, Y.; Tade, M. O.; Dai, S.; Yamauchi, Y.: Synthesis of Nitrogen-Doped Mesoporous Carbon Spheres with Extra-Large Pores through Assembly of Diblock Copolymer Micelles. *Angew. Chem. Int. Ed.* **2015**, *54*, 588-593.

(41) Tian, H.; Lin, Z.; Xu, F.; Zheng, J.; Zhuang, X.; Mai, Y.; Feng, X.: Quantitative Control of Pore Size of Mesoporous Carbon Nanospheres through the Self-Assembly of Diblock Copolymer Micelles in Solution. *Small* **2016**, *12*, 3155-3163

(42) Ding, B.; Wang, J.; Wang, Y.; Chang, Z.; Pang, G.; Dou, H.; Zhang, X.: A Two-Step Etching Route to Ultrathin Carbon Nanosheets for High Performance Electrical Double Layer Capacitors. *Nanoscale* **2016**, *8*, 11136-11142.

(43) Xiu, L.; Wang, Z.; Yu, M.; Wu, X.; Qiu, J.: Aggregation-Resistant 3D MXene-Based Architecture as Efficient Bifunctional Electrocatalyst for Overall Water Splitting. *ACS Nano* **2018**, *12*, 8017-8028.

(44) Delparastan, P.; Malollari, K. G.; Lee, H.; Messersmith, P. B.: Direct Evidence for the Polymeric Nature of Polydopamine. *Angew. Chem. Int. Ed.* **2019**, *58*, 1077-1082.

(45) Alfieri, M. L.; Micillo, R.; Panzella, L.; Crescenzi, O.; Oscurato, S. L.; Maddalena, P.; Napolitano, A.; Ball, V.; d'Ischia, M.: Structural Basis of Polydopamine Film Formation: Probing 5, 6-dihydroxyindole-Based Eumelanin Type Units and the Porphyrin Issue. *ACS Appl. Mater. Interfaces* **2017**, *10*, 7670-7680.

(46) Lee, H.; Dellatore, S. M.; Miller, W. M.; Messersmith, P. B.: Mussel-Inspired Surface Chemistry for Multifunctional Coatings. *Science* **2007**, *318*, 426-430.

(47) Jiang, J.; Zhu, L.; Zhu, L.; Zhu, B.; Xu, Y.: Surface Characteristics of a Self-Polymerized Dopamine Coating Deposited on Hydrophobic Polymer Films. *Langmuir* **2011**, *27*, 14180-14187.

(48) Young, C.; Lin, J.; Wang, J.; Ding, B.; Zhang, X.; Alshehri, S. M.; Ahamad, T.; Salunkhe, R. R.; Hossain, S. A.; Khan, J. H.; Ide, Y.; Kim, J.; Henzie, J.; Wu, K.C.W.; Kobayashi, N.; Yamauchi, Y.: Significant Effect of Pore Sizes on Energy Storage In Nanoporous Carbon Supercapacitors. *Chem. Eur. J.* **2018**, *24*, 6127-6132.

(49) Wang, J.; Tang, J.; Ding, B.; Malgras, V.; Chang, Z.; Hao, X.; Wang, Y.; Dou, H.; Zhang, X.; Yamauchi, Y.: Hierarchical Porous Carbons with Layer-by-layer Motif Architectures from Confined Soft-template Self-assembly in Layered Materials. *Nat. Commun.* **2017**, *8*, 15717.

(50) Zhu, Y.; Hu, A.; Tang, Q.; Zhang, S.; Deng, W.; Li, Y.; Liu, Z.; Fan, B.; Xiao, K.; Liu, J.; Chen, X.: Compact-Nanobox Engineering of Transition Metal Oxides with Enhanced Initial Coulombic Efficiency for Lithium-Ion Battery Anodes. *ACS Appl. Mater. Interfaces* **2018**, *10*, 8955-8964.

TOC